


Fine control of lattice thermal conductivity in low-dimensional materialsAntonio Cammarata¹* and Tomas Polcar¹*Department of Control Engineering, Faculty of Electrical Engineering, Czech Technical University in Prague, Technicka 2, 16627 Prague 6, Czech Republic* (Received 28 July 2020; revised 24 November 2020; accepted 22 December 2020; published 11 January 2021)

Optimal regulation of lattice thermal conductivity in low-dimensional materials is fundamental to obtain highly efficient miniaturized devices. To this aim, we use quantum-mechanical based analyses to understand how atomic type and structural geometry determine electron density and lattice dynamic features ruling the thermal conduction. As a case study, we consider layered van der Waals transition metal dichalcogenides with a finite number of layers. We find that a large thermal conductivity is realized when the atomic bonds display highly covalent character, promoting fast motions of the cations in correspondence of the low-frequency phonon band. Such an effect is the result of the entangled electronic and phonon features, which are captured by the covalency and cophononicity metric. The investigation protocol that we present has general applicability and can be used to design novel thermal low-dimensional materials irrespective of the kind of atomic topology and chemical composition.

DOI: [10.1103/PhysRevB.103.035406](https://doi.org/10.1103/PhysRevB.103.035406)**I. INTRODUCTION**

The technological advance of the techniques for the exfoliation or direct deposition of van der Waals materials is boosting the progress of nanotechnological devices, thanks to the possibility to access few layers of graphene, hexagonal boron nitride, and transition metal dichalcogenides (TMDs) among other low-dimensional materials [1–3]. When the device size reaches the order of tenth of nanometers, energy efficiency problems associated with heat dissipation become critical [4,5]. This pushed the development of several thermal measurement methods for nanostructured materials [6], along with experimental and theoretical investigations on the microscopic mechanisms governing the heat transfer at the nanoscale, i.e., the lattice thermal conductivity [7–9].

The lattice thermal conductivity [10] can be calculated from the direct solution to the linearized phonon Boltzmann equation [8], in which the phonon properties are optimally evaluated with *ab initio* techniques [11]. Besides the Boltzmann formulation, phonon-scattering selection rules have been identified [12–14], narrowing the study to only the relevant anharmonic processes. Such phonon-based description neglects the contributions of the electron dynamics to the total thermal conductivity; nonetheless, the average electron distribution (i.e., the static electronic density) plays a fundamental role in determining the interatomic force constants and the resulting phonon characteristics and scattering properties. The ground state electronic function is, in fact, crucial to properly describe the anharmonic interactions as shown by *ab initio* simulations of several class of materials such as semiconductors [15], aluminum oxide [16], perovskites [17,18], and

cuprates [19], especially if phonon-defect interactions or local disorder must be taken into account [20].

The connection between the electronic structure and the thermal properties is usually described in terms of the electron-phonon coupling coefficients [21]. The calculation of the latter requires the evaluation of atomic forces of thousands of configurations, each containing about 200 atoms, high-quality electronic density, and phonon perturbations of the wave function, all of them obtained by means of elaborate methods such as density functional perturbation theory [22–25]. It is then apparent that this is not a trivial task: All the steps mentioned above need a large amount of computational resources and time, besides the effort to connect all the pieces of information fragmented among the coupling coefficients and the other features of the system (e.g., geometry, atomic type, bond character, and anisotropies of the electronic density among others). Interpolation schemes based on the use of the Wannier functions may help to reduce the computational load [26]; however, the encumbrance to reduce the fragmentation of information still remains.

In the present work, we provide guidelines on how to identify possible electronic and dynamic descriptors easy to compute and able to integrate different contributions into a unitary framework. Once identified, such descriptors should be tested against the electron-phonon coupling coefficients, in order to determine their applicability conditions and limitations when used as an alternative to the coefficients in parametrizing the lattice thermal conductivity. The descriptor benchmark and the mathematical relation with the coupling constants will be the subject of a subsequent work; instead, we discuss here how the descriptors can be identified and put in relation with the thermal properties. We use a quantum-mechanical description to show how the atomic species and the structural geometry determine the subtle features of the electronic density and the lattice dynamics governing the ther-

*cammaant@fel.cvut.cz

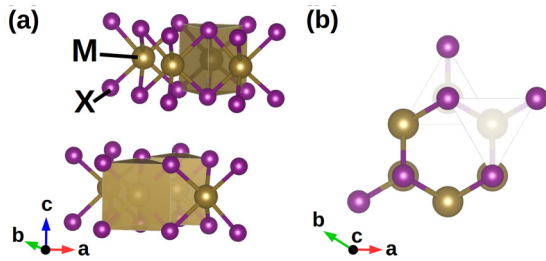


FIG. 1. Model structure of hexagonal $P6_3/mmc$ 2H polymorph of MX_2 TMD crystal. M-X bonds form trigonal prisms arranged in parallel layers separated by an interatomic gap and kept together by weak van der Waals interactions.

mal conduction at the nanoscale. To this aim, we consider lamellar van der Waals transition metal dichalcogenides as a case study with a finite number of layers. We discuss how to relate the phonon-based thermal properties with the electronic density of the ground state system and the atomic type through the use of collective descriptors; these latter might be ultimately exploited for the parametrization of several properties other than the thermal conductivity. We eventually suggest how to finely tune the lattice thermal conductivity at the nanoscale and the possibility to use the present outcomes to design novel thermal low-dimensional materials irrespective of the atomic topology and chemical composition.

II. METHODS

Transition metal dichalcogenides with general stoichiometry MX_2 are formed by transition metal cations (M) which coordinate six chalcogen anions (X) in a periodic trigonal prismatic arrangement, forming MX_2 layers with M-X covalent bonds; adjacent layers are separated by a small gap and are bound together by weak van der Waals forces (Fig. 1). We consider the 2H polymorph crystalline MX_2 compounds as reference structures [1], with $M = \text{Mo}, \text{W}$ and $X = \text{S}, \text{Se}, \text{Te}$, and hexagonal $P6_3/mmc$ symmetry (SG 194). Starting from such reference geometries, we truncate the periodic image repetition along the c axis and consider only 1, 2, 3, 4, 5, and 6 MX_2 subsequent layers by setting the c lattice parameter at 65 \AA for all the model geometries; this serves to introduce a vacuum slab parallel to the layer planes which prevents the interaction between images along the c direction. In this way, we build $6 \times 6 = 36$ model systems that we name MX_nL , where M and X specify the kind of cation and anion, respectively, while n coincides with the number of MX_2 layers present in the unit cell. The crystallographic space group of the model geometries is $P\bar{3}m1$ (#164) if n is even and $P\bar{6}m2$ (#187) if n is odd.

We perform density functional theory (DFT) calculations using the Perdew-Burke-Ernzerhof (PBE) energy functional [27] as implemented in the VASP software [28,29]. Van der Waals interactions are taken into account by using the DFT-D2 Grimme correction [30], which correctly reproduces the structural features, as we reported in previous works and references therein [31–33]. We sample the Brillouin zone with a minimum of a $7 \times 7 \times 1$ k -point mesh and plane wave cutoff of 500 eV. We report the optimized geometric

parameters in the Supplemental Material [34]. Full structural (atoms and lattice) relaxations are initiated from diffraction data [35–40] and the forces minimized to a 0.5 meV \AA^{-1} tolerance. We use the PHONOPY [41] software to diagonalize the dynamical matrices of the stable systems and compute the corresponding lattice thermal conductivity by direct solution of the linearized phonon Boltzmann equation [8] with the aid of the PHONO3PY [11] software. The values of the lattice thermal conductivity that we obtain are consistent with those reported in experimental and theoretical works [7,42]. The calculations of both second and third order force constants have been performed on supercells formed by $3 \times 3 \times 1$ primitive unit cell replicas. A $31 \times 31 \times 1$ q -point mesh was used to sample the Brillouin zone for the evaluation of the lattice thermal conductivity. Such choices are consistent with a previous convergence study on the thermal conductivity reported on the reference MX_2 bulk materials [43].

III. RESULTS AND DISCUSSION

In any solid state system, the lattice thermal conductivity tensor $\mathbb{K}(T)$ is a function of the temperature T and the phonon modes of the stable geometry according to the following relation [44]

$$\mathbb{K}(T) = \frac{1}{VN_q} \sum_{\lambda} \tau_{\lambda}(T) \mathbf{v}_{\lambda} \otimes \mathbf{v}_{\lambda} c_{\lambda}(T), \quad (1)$$

where V is the unit cell volume, N_q is the number of q points, $\tau_{\lambda}(T)$ is the relaxation time of the j th phonon mode with vector q ($\lambda = (q, j)$), \mathbf{v}_{λ} is the group velocity of the phonon λ , and $c_{\lambda}(T)$ is the mode specific heat capacity. In our case, the group velocity along the z direction ($v_{z\lambda} = \partial\omega_{\lambda}/\partial q_z$) is null because the truncation of the periodicity along the c axis makes the phonon dispersion flat along the same direction; as a consequence, any k_{iz} or k_{zi} component ($i = x, y, z$) of the \mathbb{K} tensor is null by definition [Eq. (1)]. Moreover, thanks to the symmetry operations associated to the geometries of the model systems, the only non-null elements are $k_{xx} = k_{yy}$; for this reason, we will consider only the k_{xx} component in our discussion, and all the results that we will obtain will be valid also for the k_{yy} element. We begin our analysis by observing that, irrespective of the chemical composition and at fixed number of layers n , k_{xx} is decreasing with increasing temperature [Fig. 2(a)]; this behavior is expected, since high temperatures favor a higher number of scattering processes hence a decrease of the phonon mean free path. At fixed chemical composition and irrespective of the temperature, k_{xx} is increasing with n [34], consistently with the increased number of allowed phonon recombination processes [14] [Figs. 2(b) and 2(c)]; on the other hand, at a fixed cation species, k_{xx} decreases as in the sequence $\text{S} > \text{Se} > \text{Te}$. This shows that the entangled relations among the geometric characteristics of the system (e.g., n) and the atomic kind determining the local electronic environment are then the key quantities to understand the microscopic mechanisms governing the lattice thermal conductivity. We then proceed with a detailed analysis of the physical quantities determining the final values of k_{xx} in order to identify which of them are the most relevant to control the thermal conductivity.

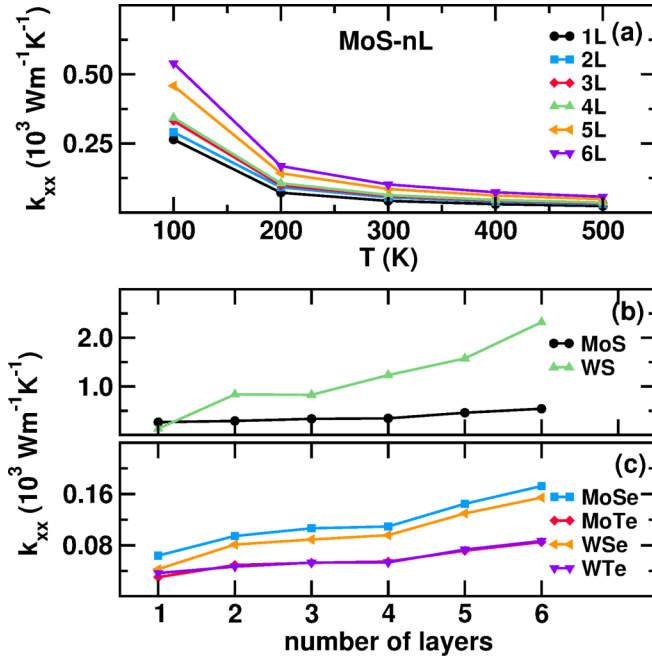


FIG. 2. (a) Lattice thermal conductivity of MoS- n L systems as a function of the temperature; similar behavior is found for all the other systems. (b),(c) Example of lattice thermal conductivity k_{xx} as a function of the number of layers: Here $T = 100 \text{ K}$, but the trend is similar at each of the considered temperature values.

Inspection of Eq. (1) suggests that one way to control \mathbb{K} is to act on the mode specific heat capacity $c_\lambda(T)$ defined as

$$c_\lambda(T) = \frac{(h\nu_\lambda)^2}{k_B T^2} \frac{\exp(h\nu_\lambda/k_B T)}{(\exp(h\nu_\lambda/k_B T) - 1)^2}, \quad (2)$$

where h and k_B are the Planck and Boltzmann constants, respectively, while ν_λ is the eigenfrequency of the mode λ . This relation is based on the equilibrium distribution of noninteracting harmonic phonons and is not affected by the phonon coupling; nonetheless, the latter is crucial for the thermal transport phenomenon to occur. For this reason, $c_\lambda(T)$ cannot provide the physical insights that we are looking for and we will not consider it any further in our analysis. Another way to modify \mathbb{K} is to tune the group velocity v_λ ; indeed, this has already been achieved by inducing strain on the pristine structure via ion intercalation in the interlayer region, or by applying an external pressure [43,45,46]. In our systems, we observe that k_{xx} is monotonically increasing with the cumulative norm of group velocity at fixed composition, consistently with the fact that the latter linearly increases with n . However, also the group velocity does not provide much details on the entangled features of the systems determining the thermal transport such as electronic density, frequency dispersion, and phonon coupling. We will then continue our analysis by focusing only on the phonons contribution to k_{xx} through the relaxation time τ_λ . To identify which phonons are relevant to k_{xx} , we consider the quantity $\partial k_{xx}/\partial \nu$, which is a measure of how the phonon modes per frequency interval determine the variation of k_{xx} . In our finite systems we observe that, irrespective of the atomic type, the number of layers, and the temperature, the main contribution to the lattice thermal

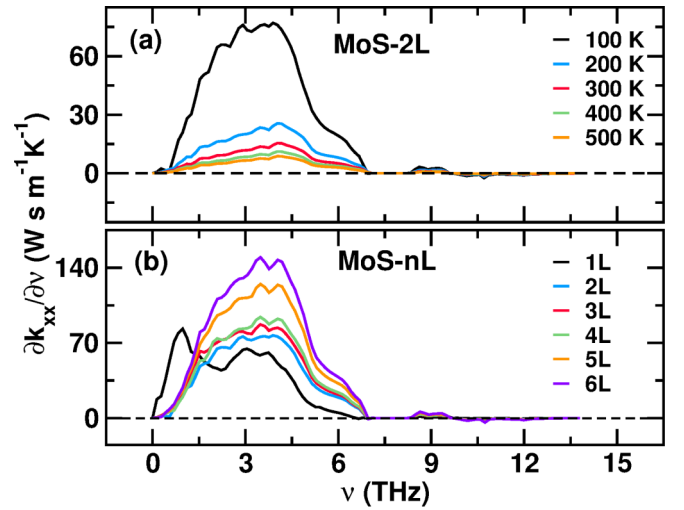


FIG. 3. Phonon contribution to the lattice thermal conductivity per frequency unit for (a) the MoS-2L system at different temperatures and (b) the MoS- n L system at $T = 100 \text{ K}$. Similar behavior is found for all the other systems at varying temperature or number of layers.

conductivity comes from the phonons in the low frequency band below the band gap [34] (Fig. 3). At fixed atomic species and n , the contribution to k_{xx} per frequency decreases with increasing temperature [Fig. 3(a)]; this explains the origin of the trends shown in Fig. 2(a). Analogously, at fixed composition and temperature, the phonon contribution increases with increasing number of layers [Fig. 3(b)], accounting for the variation of k_{xx} with n as we report in Figs. 2(b) and 2(c).

To discuss the dependence of k_{xx} from τ_λ , we then consider the cumulative phonon lifetime τ integrated over the low frequency band:

$$\tau = \int_0^{\nu_g} \frac{1}{N_q} \sum_\lambda \tau_\lambda \delta(\nu_\lambda - \nu') d\nu', \quad (3)$$

where ν_g is the frequency value corresponding to the top of the low-frequency band and $\delta(\nu_\lambda - \nu')$ is the Dirac delta. We observe that, at a fixed composition and irrespective of the temperature, k_{xx} is increasing with τ which, in turn, increases with the number of layers (Fig. 4); a little deviation is found for the MoS-6L compound but this does not influence the global trends and then our final conclusions. In general, the width of the band gap affects the phonon lifetime, hence the lattice thermal conductivity; however, no clear trend of k_{xx} with the band gap is observed. Moreover, the band gap itself contains both electronic and dynamic (i.e., phonon) contributions in an entangled way, while we are here interested in the isolation of such contributions which determine the relaxation time τ_λ , and finally connect them to the lattice thermal conductivity.

The phonon lifetime τ_λ depends on the phonon-phonon scattering processes and the temperature via the following

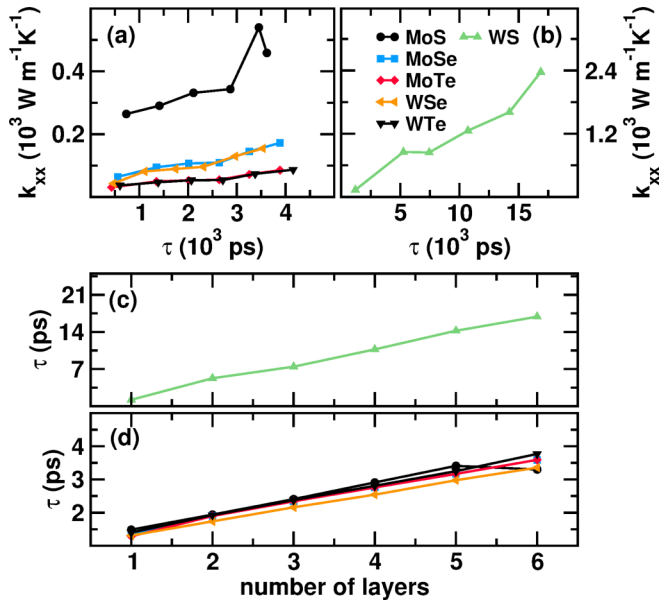


FIG. 4. (a), (b) Lattice thermal conductivity as a function of the cumulative phonon lifetime and (c), (d) cumulative phonon lifetime as a function of the number of layers. The legend is common to all the subfigures. The shown data are simulated at $T = 100 \text{ K}$ but analogous behavior is found for all the other considered temperature values.

relation [47]:

$$\begin{aligned} \tau_{\lambda}^{-1}(T) \propto & \sum_{\lambda'\lambda''} |\Phi_{-\lambda\lambda'\lambda''}|^2 \{ (n_{\lambda'} + n_{\lambda''} + 1) \\ & \times \delta(\omega_{\lambda} - \omega_{\lambda'} - \omega_{\lambda''}) + (n_{\lambda'} - n_{\lambda''}) \\ & \times [\delta(\omega_{\lambda} + \omega_{\lambda'} - \omega_{\lambda''}) - \delta(\omega_{\lambda} - \omega_{\lambda'} + \omega_{\lambda''})] \}, \end{aligned} \quad (4)$$

where the Dirac delta guarantees the energy conservation, the temperature dependence is contained in the phonon populations n_{λ} and $n_{\lambda''}$, and the three-phonon interaction strength $\Phi_{\lambda\lambda'\lambda''}$ tensor contains the effect of the atomic type, the geometry, the electronic density, and the phonon dynamics on the determination of the thermal conductivity. The third order tensor $\Phi_{\lambda\lambda'\lambda''}$ is therefore an intrinsic characteristic of the system as it is defined as [44,47]

$$\begin{aligned} \Phi_{\lambda\lambda'\lambda''} \propto & \frac{1}{\sqrt{\omega_{\lambda}\omega_{\lambda'}\omega_{\lambda''}}} \sum_{kk'k''} \frac{1}{\sqrt{m_k m_{k'} m_{k''}}} \\ & \times \sum_{\alpha\beta\gamma} e_{\lambda}^{\alpha}(\mathbf{r}_k) e_{\lambda'}^{\beta}(\mathbf{r}_{k'}) e_{\lambda''}^{\gamma}(\mathbf{r}_{k''}) \\ & \times \sum_{l'l''} e^{iq\cdot\mathbf{r}_{kl}} e^{iq'\cdot\mathbf{r}_{k'l'}} e^{iq''\cdot\mathbf{r}_{k''l''}} \Phi_{\alpha\beta\gamma}(\mathbf{r}_{kl}, \mathbf{r}_{k'l'}, \mathbf{r}_{k''l''}), \end{aligned} \quad (5)$$

where ω_{λ} is the eigenfrequency of the mode λ , m_k is the mass of the k th atom, \mathbf{r}_k ($\mathbf{r}_{k'l'}$, $\mathbf{r}_{k''l''}$) is the position of the k th (k' th, k'' th) atom in the l th (l' th, l'' th) cell replica, $e_{\lambda}^{\alpha}(\mathbf{r}_k)$ is the α th cartesian component of the eigenvector associated to the mode λ and to the k th atom, and $\Phi_{\alpha\beta\gamma}$ is the third-rank cartesian tensor of the cubic anharmonic force constants. The force constants, in turn, depend on the type of atoms

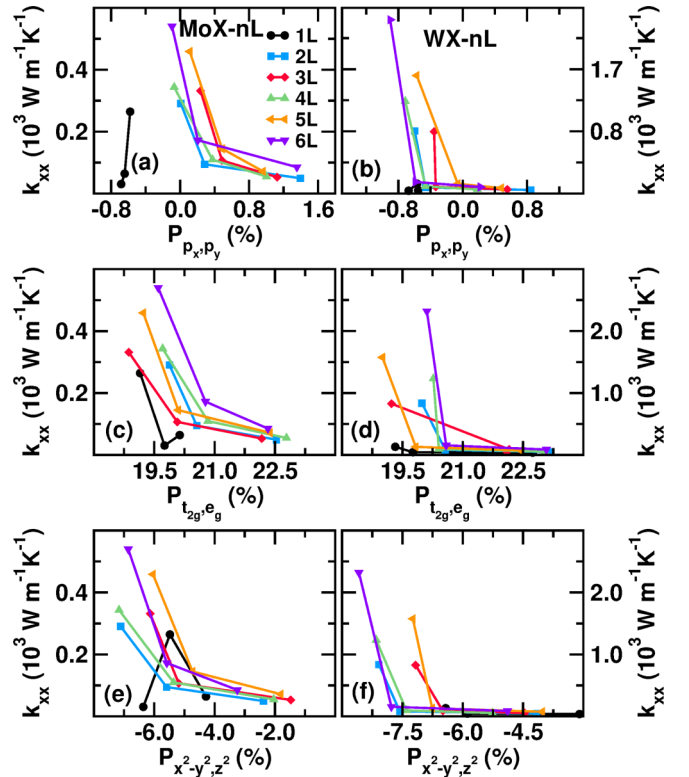


FIG. 5. Lattice thermal conductivity as a function of the orbital polarization of the MoX- n L (left panels) and WX- n L structures (right panels) calculated by considering (a), (b) the p_x , p_y orbitals of the X anion, while (c), (d) t_{2g} , e_g and (e), (f) $d_{x^2-y^2}$, d_{z^2} orbitals are centered on the M cation. The legend is common to all the subfigures. The shown k_{xx} data are simulated at $T = 100 \text{ K}$ but analogous behavior is found for all the other considered temperature values.

and the topologic environment in which they are embedded and manifest themselves as specific spatial distributions of the electronic density, the degree of bond covalency, and the vibrational properties of the lattice. The phonon scattering is then determined by the atomic kinds and geometry forming the system which, in turn, determine eigenvectors, eigenfrequencies, and interatomic force constants. Therefore, k_{xx} is regulated by the electronic and dynamic features of the system through the square modulus of multiple $\Phi_{\lambda\lambda'\lambda''}$ elements. In order to capture those features into a unitary framework, we will then make use of general descriptors such as orbital polarization [33,48–50], M-X bond covalency [51,52], and M-X pair cophoncity [31,52,53].

The orbital polarization $\mathcal{P}_{lm,l'm'}$ is able to quantify the local spatial anisotropies of the electronic distribution: the larger the value, the larger the excess of charge in the $|lm\rangle$ orbital with respect to the $|l'm'\rangle$ orbital. We consider the p_x and p_y orbitals centered onto the anion sites to evaluate the \mathcal{P}_{p_x, p_y} orbital polarization, while the t_{2g} , e_g , $d_{x^2-y^2}$, and d_{z^2} orbitals associated to the cation are used to calculate the $\mathcal{P}_{t_{2g}, e_g}$ and $\mathcal{P}_{x^2-y^2, z^2}$ values, respectively. We observe that, at a fixed number of layers and kind of cation, k_{xx} monotonically decreases with all of the three considered orbital polarizations (Fig. 5); at the same time, we observe that k_{xx} monotonically increases with the covalent character of the M-X bond (Fig. 6).

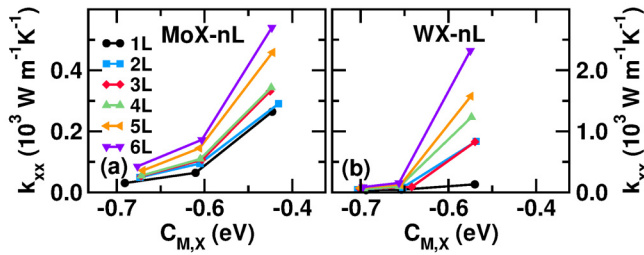


FIG. 6. Lattice thermal conductivity as a function of the M-X bond covalency for the (a) MoX- n L and (b) WX- n L systems. Legend is common to all the subfigures. The shown k_{xx} data are simulated at $T = 100$ K but analogous behavior is found for all the other considered temperature values.

Indeed, orbital polarizations and covalency are strongly related: We already observed that high values of the orbital polarizations determine the formation of more ionic M-X bonds in finite MX_2 systems [54]. We can therefore conclude that more covalent bonds favor a larger thermal conductivity across the lattice. We notice that k_{xx} is not monotonic with the orbital polarization only in the three MoX-1L systems; this behavior is then peculiar of only the Mo-based structures formed by one MoX_2 layer. However this exception does not affect the covalency trend and our conclusions on the influence of the covalent character on the thermal conductivity. Previous works on cubic systems already showed how \mathbb{K} is influenced by the bond character, whereas the latter has been qualitatively assessed by considerations on harmonic quantities like the acoustic Debye temperature [55,56]; in this way, dynamic quantities have been used to characterize one of the aspects of the electronic distribution under specific symmetry assumptions. Instead, it is the electronic distribution that determines the force constants via the Hellmann-Feynman theorem, which in turn determine the dynamical matrix, then the phonon dispersion and thus finally the group velocities and the related quantities. For this reason, we here provide a quantitative measure of the bond covalency and the phonon properties as independent quantities, both being two different manifestations of the features of the electronic distribution. A possible route to engineer the thermal conductivity is then to tune the bond covalency through a fine control of the orbital polarization; this can be achieved with proper choices of atomic species [33], local distortions [49], or induced charge unbalance [48].

We now calculate the cophonycity $C_{\text{ph}}(\text{M-X})$ of the M-X pair in the range of the low-frequency band $[0, \nu_g]$ that we individuated with the analysis of the phonon contribution presented above (Fig. 3). Positive $C_{\text{ph}}(\text{M-X})$ values mean that the M and X atoms contribute more to the higher- and lower-frequency displacements within the integration interval, respectively; this corresponds to an average faster motion of the M than the X atoms when forming the global atomic motions; the opposite holds for negative $C_{\text{ph}}(\text{M-X})$ values. A cophonycity close to zero corresponds to atomic displacements in which both atomic species move in average at the same velocity. We first observe that cophonycity is nearly constant with the number of layers at each chemical com-

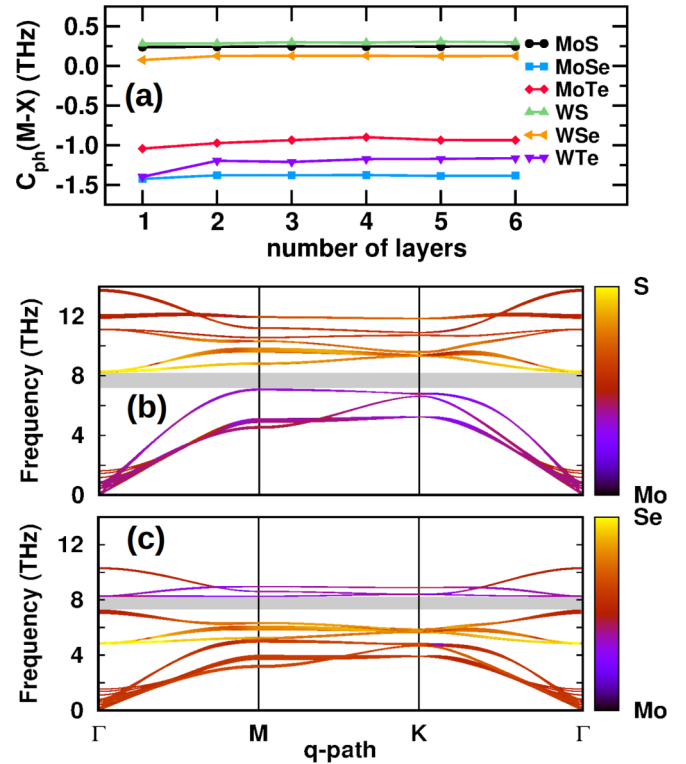


FIG. 7. (a) Cophonycity of the M-X pair as a function of the number of layers. (b) Phonon band structure of MoS-6L system along a linear path joining the high symmetry points of the irreducible Brillouin zone. The band gap present in the interval [7.1,8.1] THz separates the low from the high frequency band. The color gradient indicates the atomic character of the phonon displacements: Mo (S) atoms displacements are larger than those of S (Mo) atoms for nearly all the phonon modes forming the low (high) frequency band. Opposite behavior is observed for the (c) MoSe-6L system, where the anion character is predominant in the upper part of the low-frequency band corresponding to the interval [7.3, 8.1] THz. The light-gray area in (b) and (c) highlights the band gap; the phonon dispersions about the Γ point display a quadratic trend as expected from the theory [57].

position [Fig. 7(a)]; in this respect, it can be regarded as an intrinsic feature of the M-X pair type forming the structure. The MoS- n L, WS- n L, and WSe- n L systems are characterized by a positive cophonycity, then the cation motions are predominant in the top part of the low-frequency band; the opposite holds for the remaining compounds. This is apparent if we consider the atom character of the phonon modes [34]. As an example, we report the atom character of the band dispersion of the MoS-6L system along a linear path joining the high-symmetry points in the irreducible Brillouin zone (IBZ): The Mo components of the eigendisplacements are predominant in the low-frequency band, while the opposite holds for the S components [Fig. 7(b)]. This means that when the atoms displace according to the low-band phonon eigenvectors, the Mo atoms have largest displacements compared than those of the S atoms. Focusing on the low-frequency band which is the one relevant for our purposes, the top part of it has a predominant Mo character with respect to the bottom part, in agreement with the cophonycity value. Conversely,

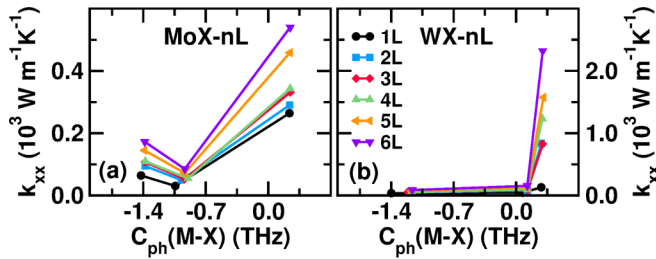


FIG. 8. Lattice thermal conductivity as a function of the M-X pair cophonycity for the (a) MoX-*n*L and (b) WX-*n*L systems. Legend is common to both subfigures. The shown k_{xx} data are simulated at $T = 100$ K but analogous behavior is found for all the other considered temperature values.

in the MoSe-6L system, the anion character is dominant in the top part of the low-frequency band [Fig. 7(c)]. In this respect, cophonycity is a convenient metric to parametrize the phonon character, especially when considering uniform sampling in the IBZ, which is the case of lattice thermal conductivity calculations. We observe that k_{xx} is increasing with cophonycity [Figs. 8(a) and 8(b)]: This suggests that thermal conduction is favored when the vibrational atomic motions have a predominant M character in the upper part of the lower phonon band. Another possible way to engineer the thermal conductivity is then to control the atomic character of the phonons via the M-X pair cophonycity. Larger cophonycity values are realized when covalency is the maximum possible among the considered compounds, irrespective of the number of layers and at fixed kind of cation (Fig. 9). By a proper choice of the atomic species, it is then possible to adjust the M-X bond character and the cophonycity, in order to obtain the desired lattice thermal conductivity. Indeed, we already observed how a specific $\text{Ti} \rightarrow \text{Mo}$ cation substitution in MoS₂-based compounds induces local distortions which regulate the bond covalency [31] or the phonon symmetries [14], the latter dictating which dissipation channels are active in the system.

At this point, it would be desirable to have a mathematical expression of \mathbb{K} in terms of the orbital \mathcal{P} polarization and the C_{ph} cophonycity; certainly, this is possible by considering the decomposition of the system wave function into hydrogenlike atom-centered $|lm\rangle$ orbitals. In fact, \mathbb{K} depends on $\Phi_{\lambda\lambda'\lambda''}$ [Eqs. (1) and (4)], which is the Fourier transform of the third-order interatomic force constants [Eq. (5)]. The phonon eigenvectors e_{λ} , entering in the definition of $\Phi_{\lambda\lambda'\lambda''}$,

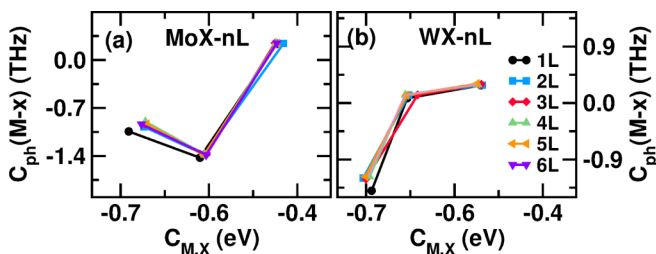


FIG. 9. Cophonycity as a function of covalency for (a) MoX-*n*L and (b) WX-*n*L systems, respectively. Larger values of covalency realize larger cophonycity values.

are eigenvectors of the dynamical matrix, which is the Fourier transform of the second-order interatomic force constants [44,47]. The second- and third-order force constants, in turn, are calculated from the forces acting on the atoms displaced from the equilibrium position [58,59]; they thus depend on the system wave function $|\Psi\rangle$ via the Hellmann-Feynman theorem [60]. The eigenvectors, eigenfrequencies, and $\Phi_{\lambda\lambda'\lambda''}$ can therefore be written in terms of $|lm\rangle$ orbitals by using the latter as a basis to express $|\Psi\rangle$: $|\Psi\rangle = \sum \langle lm|\Psi\rangle |lm\rangle$. Moreover, the phonon eigenfrequencies enter in the definition of the cophonycity via the phonon density of states; this means that the cophonycity can also be written as a function of the $|lm\rangle$ orbitals. By substituting the wave-function dependence for the quantities appearing in the definition of $\Phi_{\lambda\lambda'\lambda''}$, orbital polarization and cophonycity, it is then possible to obtain an explicit mathematical expression which relates the lattice thermal conductivity to the orbital polarization and cophonycity. However, the final $k_{xx} = f(\mathcal{P}(|lm\rangle), C_{\text{ph}}(|lm\rangle))$ formulation might need to be evaluated numerically, this depending on the functional form of the Hamiltonian. It is then apparent that this is not a trivial task and will be the subject of our future work mentioned in the introduction section.

The lattice thermal conductivity \mathbb{K} of a solid state system is then connected to the electronic (e.g., covalency) and dynamic (e.g., cophonycity) features via the third order phonon-phonon interaction strength tensor; in principle, we could have then looked at how any variation of the $\Phi_{\lambda\lambda'\lambda''}$ elements would have determined possible changes of the k_{xx} values. This is a useful approach if one wants to isolate selected energy flow channels to locally engineer the direction of the heat flux; in such a case, a detailed analysis of the mode symmetries [14] and/or specific $\Phi_{\lambda\lambda'\lambda''}$ elements [54] would be required. However, with the present work, we aimed to control the thermal conductivity via global features, without losing the general overview due to an excessive fragmentation of information: For this reason, such detailed analysis was not necessary and we achieved our goal by individuating the covalency and cophonycity as potential useful descriptors which encompass all the needed electronic and dynamic details. We already observed that covalency, and hence the orbital polarization, can be tuned by finely adjusting the atom topology, geometric distortions and/or by ion substitution [31,33,54]. Moreover, these descriptors can be used in machine learning engines [61] for automated research of novel thermal materials with targeted characteristics. We finally notice that the use of such descriptors and the recognition of allowed scattering channels by means of selection rules are faster and less computationally demanding than the evaluation of the electron-phonon coupling constants or the $\Phi_{\lambda\lambda'\lambda''}$ tensor. Indeed, the latter requires the calculation of atomic forces of thousands of configurations, together with triple scalar products with phonon eigenvectors over a grid of thousands of \mathbf{q} points [11,43,44], with a computational load comparable to that needed to calculate the electron-phonon coupling constants.

IV. CONCLUSIONS

We studied the relation among the lattice thermal conductivity, the electron distribution, and the phonon modes of prototypical layered transition metal dichalcogenides. The

bridging quantity is identified in the phonon-phonon interaction strength tensor $\Phi_{\lambda\lambda'\lambda''}$ which rules the scattering processes responsible of the thermal conduction. The $\Phi_{\lambda\lambda'\lambda''}$ tensor is an intrinsic property of the system, since it depends on the atomic kinds and topology which, in turn, determine phonon eigenvectors, eigenfrequencies, and interatomic force constants. The atomic types and the induced electronic local environment are then the key quantities to control in order to design thermal materials with targeted properties. We find that specific anisotropies in the electronic environment and corresponding highly covalent bonds favor larger thermal conductivity across the lattice. The bond character is also tied to distinct features of the lattice dynamics, the latter being peculiar of the chemical composition and independent of the structural geometry (i.e., the number of layers). In fact, from the analysis of the atomic participation to the eigendisplacements, we understand that a large thermal conductivity is favored when the cation motion is predominant in the top part of the low-frequency phonon band. This aspect is quantified with the cophononicity metric which can be regarded as a measure for the dynamical effect of the

atomic type on the environment in which it is embedded. Finally, the simple relations between those descriptors and the thermal conductivity constitute a quick and convenient guide in the design of thermal materials. Benchmarks against the electron-phonon coupling coefficients would determine their applicability conditions and limitations, ultimately promoting them as parameters that can be used for fast screening of large databases, or in machine learning engines, aimed to identify promising thermal materials.

ACKNOWLEDGMENTS

This work has been done with the support of the Czech Science Foundation (Project No. 17-24164Y) and the project “Novel nanostructures for engineering applications” No. CZ.02.1.01/0.0/0.0/16_026/0008396. This work was supported by The Ministry of Education, Youth and Sports from the Large Infrastructures for Research, Experimental Development and Innovations project “e-Infrastructure CZ-LM2018140.” The use of VESTA [62] software is also acknowledged.

-
- [1] M. Chhowalla, H. S. Shin, G. Eda, L.-J. Li, K. P. Loh, and H. Zhang, *Nat. Chem.* **5**, 263 (2013).
- [2] Y.-M. Lin, C. Dimitrakopoulos, K. A. Jenkins, D. B. Farmer, H.-Y. Chiu, A. Grill, and P. Avouris, *Science* **327**, 662 (2010).
- [3] Y.-G. Choi, D.-G. Jeong, H. I. Ju, C. J. Roh, G. Kim, B. S. Mun, T. Y. Kim, S.-W. Kim, and J. S. Lee, *Sci. Rep.* **9**, 7612 (2019).
- [4] R. Courtland, *IEEE Spectrum* **54**, 52 (2017).
- [5] E. Pop, *Nano Res.* **3**, 147 (2010).
- [6] Y. Wang, N. Xu, D. Li, and J. Zhu, *Adv. Funct. Mater.* **27**, 1604134 (2017).
- [7] C. Muratore, V. Varshney, J. J. Gengler, J. J. Hu, J. E. Bultman, T. M. Smith, P. J. Shamberger, B. Qiu, X. Ruan, A. K. Roy, and A. A. Voevodin, *Appl. Phys. Lett.* **102**, 081604 (2013).
- [8] L. Chaput, *Phys. Rev. Lett.* **110**, 265506 (2013).
- [9] Z.-Y. Ong and M.-H. Bae, *2D Materials* **6**, 032005 (2019).
- [10] J. Ranninger, *Phys. Rev.* **140**, A2031 (1965).
- [11] A. Togo, L. Chaput, and I. Tanaka, *Phys. Rev. B* **91**, 094306 (2015).
- [12] L. Lindsay, D. A. Broido, and N. Mingo, *Phys. Rev. B* **80**, 125407 (2009).
- [13] L. Lindsay, D. A. Broido, and N. Mingo, *Phys. Rev. B* **82**, 115427 (2010).
- [14] A. Cammarata, *RSC Adv.* **9**, 37491 (2019).
- [15] J. M. Skelton, D. Tiana, S. C. Parker, A. Togo, I. Tanaka, and A. Walsh, *J. Chem. Phys.* **143**, 064710 (2015).
- [16] B. Dongre, J. Carrete, N. Mingo, and G. K. Madsen, *MRS Communications* **8**, 1119 (2018).
- [17] H. Dekura, T. Tsuchiya, and J. Tsuchiya, *Phys. Rev. Lett.* **110**, 025904 (2013).
- [18] A. O. Fumega, Y. Fu, V. Pardo, and D. J. Singh, *Phys. Rev. Materials* **4**, 033606 (2020).
- [19] J. Linnera and A. J. Karttunen, *Phys. Rev. B* **96**, 014304 (2017).
- [20] L. Lindsay, A. Katre, A. Cepellotti, and N. Mingo, *J. Appl. Phys.* **126**, 050902 (2019).
- [21] D. Gerald, *Many-Particle Physics*, 3rd ed. (Kluwer Academic, Plenum Publishers, New York, 2000), p. 785.
- [22] Z. Tong, S. Li, X. Ruan, and H. Bao, *Phys. Rev. B* **100**, 144306 (2019).
- [23] D. D. Fan, H. J. Liu, L. Cheng, J. H. Liang, and P. H. Jiang, *J. Mater. Chem. A* **6**, 12125 (2018).
- [24] X. Gonze, B. Amadon, G. Antonius, F. Arnardi, L. Baguet, J.-M. Beuken, J. Bieder, F. Bottin, J. Bouchet, E. Bousquet, N. Brouwer, F. Bruneval, G. Brunin, T. Cavignac, J.-B. Charraud, W. Chen, M. Côté, S. Cottenier, J. Denier, G. Geneste *et al.*, *Comput. Phys. Commun.* **248**, 107042 (2020).
- [25] S. Yabuuchi, Y. Kurosaki, N. Fukatani, and J. Hayakawa, *Materials Today: Proceedings* (2020), doi:10.1016/j.matpr.2020.02.386.
- [26] J. Noffsinger, F. Giustino, B. D. Malone, C.-H. Park, S. G. Louie, and M. L. Cohen, *Comput. Phys. Commun.* **181**, 2140 (2010).
- [27] J. P. Perdew, K. Burke, and M. Ernzerhof, *Phys. Rev. Lett.* **77**, 3865 (1996).
- [28] G. Kresse and J. Furthmüller, *Comp. Mater. Sci.* **6**, 15 (1996).
- [29] G. Kresse and D. Joubert, *Phys. Rev. B* **59**, 1758 (1999).
- [30] S. Grimme, *J. Comp. Chem.* **27**, 1787 (2006).
- [31] A. Cammarata and T. Polcar, *Inorg. Chem.* **54**, 5739 (2015).
- [32] A. Cammarata and T. Polcar, *RSC Adv.* **5**, 106809 (2015).
- [33] A. Cammarata and T. Polcar, *Phys. Chem. Chem. Phys.* **18**, 4807 (2016).
- [34] See Supplemental Material at <http://link.aps.org/supplemental/10.1103/PhysRevB.103.035406> for the sections Optimized structures of the MX-nL systems; Lattice thermal conductivity as a function of the temperature; Lattice thermal conductivity as a function of the number of layers; Phonon contribution to the lattice thermal conductivity; and Atomic character of the phonon modes.
- [35] B. Schönfeld, J. J. Huang, and S. C. Moss, *Acta Crystallogr. B* **39**, 404 (1983).
- [36] V. Kalikhman, *Inorg. Mater.* **19**, 957 (1983).
- [37] L. Brixner, *J. Inorg. Nucl. Chem.* **24**, 257 (1962).

- [38] W. Schutte, J. D. Boer, and F. Jellinek, *J. Solid State Chem.* **70**, 207 (1987).
- [39] V. L. Kalikhman, *Neorganicheskie Materialy* **19**, 1060 (1983).
- [40] A. A. Yanaki and V. A. Obolonchik, *Inorg. Mater.* **9**, 1855 (1973).
- [41] A. Togo, F. Oba, and I. Tanaka, *Phys. Rev. B* **78**, 134106 (2008).
- [42] A. Mobaraki, C. Sevik, H. Yapicioglu, D. Çakir, and O. Gülseren, *Phys. Rev. B* **100**, 035402 (2019).
- [43] D. O. Lindroth and P. Erhart, *Phys. Rev. B* **94**, 115205 (2016).
- [44] J. M. Ziman, *Electrons and Phonons: The Theory of Transport Phenomena in Solids* (Oxford University Press, London, UK, 2001).
- [45] S. Chen, A. Sood, E. Pop, K. E. Goodson, and D. Donadio, *2D Materials* **6**, 025033 (2019).
- [46] X. Meng, T. Pandey, J. Jeong, S. Fu, J. Yang, K. Chen, A. Singh, F. He, X. Xu, J. Zhou, W.-P. Hsieh, A. K. Singh, J.-F. Lin, and Y. Wang, *Phys. Rev. Lett.* **122**, 155901 (2019).
- [47] D. M. Wallace, *Thermodynamics of Crystals* (John Wiley & Sons Inc., New York, 1972).
- [48] A. Cammarata and T. Polcar, *Nanoscale* **9**, 11488 (2017).
- [49] A. Cammarata and J. M. Rondinelli, *Phys. Rev. B* **87**, 155135 (2013).
- [50] M. J. Han, C. A. Marianetti, and A. J. Millis, *Phys. Rev. B* **82**, 134408 (2010).
- [51] A. Cammarata and J. M. Rondinelli, *J. Chem. Phys.* **141**, 114704 (2014).
- [52] R. Fei, W. Kang, and L. Yang, *Phys. Rev. Lett.* **117**, 097601 (2016).
- [53] A. A. Tedstone, D. J. Lewis, and P. O'Brien, *Chem. Mater.* **28**, 1965 (2016).
- [54] A. Cammarata and T. Polcar, *Phys. Rev. B* **102**, 085409 (2020).
- [55] G. Slack, *J. Phys. Chem. Solids* **34**, 321 (1973).
- [56] S. Lee, K. Esfarjani, T. Luo, J. Zhou, Z. Tian, and G. Chen, *Nat. Commun.* **5**, 3525 (2014).
- [57] J. Carrete, W. Li, L. Lindsay, D. A. Broido, L. J. Gallego, and N. Mingo, *Mater. Res. Lett.* **4**, 204 (2016).
- [58] L. Chaput, A. Togo, I. Tanaka, and G. Hug, *Phys. Rev. B* **84**, 094302 (2011).
- [59] K. Parlinski, Z. Q. Li, and Y. Kawazoe, *Phys. Rev. Lett.* **78**, 4063 (1997).
- [60] R. P. Feynman, *Phys. Rev.* **56**, 340 (1939).
- [61] F. Belviso, V. E. P. Claerbout, A. Comas-Vives, N. S. Dalal, F.-R. Fan, A. Filippetti, V. Fiorentini, L. Foppa, C. Franchini, B. Geisler, L. M. Ghiringhelli, A. Groß, S. Hu, J. Áñíguez, S. K. Kauwe *et al.*, *Inorg. Chem.* **58**, 14939 (2019).
- [62] K. Momma and F. Izumi, *J. Appl. Crystallogr.* **44**, 1272 (2011).